

distribution of FDG in the myocardium was observed in fasting and severe hyperglycemic states. FDG uptake by skeletal muscles showed a pattern similar to that of the myocardium. Understanding of these FDG uptake characteristics and their dependence on blood glucose is helpful in interpreting myocardial FDG-PET scans.

ACKNOWLEDGMENTS

We thank the staff of the Cyclotron and Radioisotope Center Tohoku University for their cooperation, Mr. Y. Sugawara for photography, Professors H. Fukuda and T. Ido for their support and Dr. A. Fukao for statistical assistance. We also thank Dr. F.G., Issa University of Sydney, Australia, for editorial assistance. This work was supported by grants-in-aid 06454320, 06670899, 07274206 from the Japanese Ministry of Education, Science and Culture.

REFERENCES

- Schwaiger M, Hicks R. The clinical role of metabolic imaging of the heart by positron emission tomography. *J Nucl Med* 1991;32:565-578.
- Camici P, Ferrannini E, Opie LH. Myocardial metabolism in ischemic heart disease: basic principles and application to imaging by positron emission tomography. *Prog Cardiovasc Dis* 1989;32:217-238.
- Yamada K, Endo S, Fukuda H, et al. Experimental studies on myocardial glucose metabolism of rats with ^{18}F -2-fluoro-2-deoxy-D-glucose. *Eur J Nucl Med* 1985;10:341-345.
- Knuuti MJ, Nuutila P, Ruotsalainen U, et al. Euglycemic hyperinsulinemic clamp and oral glucose load in stimulating myocardial glucose utilization during positron emission tomography. *J Nucl Med* 1992;33:1255-1262.
- Gropler RJ, Siegel BA, Lee KJ, et al. Nonuniformity in myocardial accumulation of fluorine-18-fluorodeoxyglucose in normal, fasted humans. *J Nucl Med* 1990;31:1749-1756.
- Voipio-Pulkki LM, Nuutila P, Knuuti MJ, et al. Heart and skeletal muscle glucose disposal in type 2 diabetic patients as determined by positron emission tomography. *J Nucl Med* 1993;34:2064-2067.
- Rerup CC. Drugs producing diabetes through damage of the insulin secreting cells. *Pharmacol Rev* 1970;22:485-518.
- Mooradian AD. Effect of ascorbate and dehydroascorbate on tissue uptake of glucose. *Diabetes* 1987;36:1001-1004.
- Pecoraro RE, Chen MS. Ascorbic acid metabolism in diabetes mellitus. *Ann NY Acad Sci* 1987;498:248-257.
- Camici P, Araujo LI, Spinks T, et al. Increased uptake of ^{18}F -fluorodeoxyglucose in posts ischemic myocardium of patients with exercised-induced angina. *Circulation* 1986;74:81-88.
- Kubota K, Matsuzawa T, Fujiwara T, et al. Differential diagnosis of AH109A tumor and inflammation by radioscinigraphy with L-[methyl ^{11}C]methionine. *Jpn J Cancer Res* 1989;80:778-782.
- Sugden MC, Holness MJ, Liu Y-L, Smith DM, Fryer LG, Kurszynska YT. Mechanisms regulating cardiac fuel selection in hyperthyroidism. *Biochem J* 1992;286:513-517.
- Bonen A, Megoney LA, McCarthy SC, McDermott JC, Tan MH. Epinephrine administration stimulates Glut-4 translocation but reduces glucose transport in muscle. *Biochem Biophys Res Commun* 1992;187:685-691.
- Lozeman FJ, Challiss RAJ, Leighton B, Newsholme EA. Effects of dipyridamole on adenosine concentration, insulin sensitivity and glucose utilization in soleus muscle of the rat. *Eur J Physiol* 1987;410:192-197.
- Amatruda JM, Livingston JN, Lockwood DH. Cellular mechanisms in selected states of insulin resistance: human obesity, glucocorticoid excess and chronic renal failure. *Diabetes Metab Rev* 1985;1:293-317.
- Wahlqvist ML, Lim SP, Shanahan EA, Outch K. Role of cortisol in cardiac glucose metabolism in vivo. *Advances in Myocardiology*, 1980;2:39-50.
- Haber RS, Weinstein SP. Role of glucose transporters in glucocorticoid-induced insulin resistance: Glut-4 isoform in rat skeletal muscle is not decreased by dexamethasone. *Diabetes* 1992;41:728-735.
- Bennett RA, Pegg AE. Alkylation of DNA in rat tissues following administration of streptozotocin. *Cancer Res* 1981;41:2786-2790.
- Kahn BB, Flier JS. Regulation of glucose-transporter gene expression in vitro and in vivo. *Diabetes Care* 1990;13:548-564.
- Kahn BB, Rossetti L, Lodish HF, Charron MJ. Decreased in vivo glucose uptake but normal expression of Glut-1 and Glut-4 in skeletal muscle of diabetic rats. *J Clin Invest* 1991;87:2197-2206.
- Kainulainen H, Breiner M, Schürmann A, Martinen A, Virjo A, Joost HG. In vivo glucose uptake and glucose transporter proteins Glut-1 and Glut-4 in heart and various types of skeletal muscle from streptozotocin-diabetic rats. *Biochim Biophys Acta* 1994;1225:275-282.
- Garvey WT, Hardin D, Juhaszova M, Dominguez JH. Effects of diabetes on myocardial glucose transport system in rats: implications for diabetic cardiomyopathy. *Am J Physiol* 1993;264:H837-H844.
- Ng CK, Holden JE, DeGrado TR, Raffel DM, Kornguth ML, Gatley SJ. Sensitivity of myocardial fluorodeoxyglucose lumped constant to glucose and insulin. *Am J Physiol* 1991;260:H593-H603.
- Hariharan R, Bray M, Ganim R, Doenst T, Goodwin GW, Taegtmeier H. Fundamental limitation of [^{18}F]2-deoxy-2-fluoro-D-glucose for assessing myocardial glucose uptake. *Circulation* 1995;91:2435-2444.
- Clarke K, Veech RL. Metabolic complexities in cardiac imaging. *Circulation* 1995;91:2299-2301.

Derivation of Input Function from FDG-PET Studies in Small Hearts

Hsiao-Ming Wu, Sung-Cheng Huang, Vivekanand Allada, Peter J. Wolfenden, Heinrich R. Schelbert, Michael E. Phelps and Carl K. Hoh

Division of Nuclear Medicine and Biophysics, Department of Molecular and Medical Pharmacology, Laboratory of Structural Biology and Molecular Medicine; and Division of Cardiology, Department of Pediatrics, University of California at Los Angeles, School of Medicine, Los Angeles, California

The extraction of pure arterial time-activity curves (TACs) from dynamic PET images of a small animal heart using factor analysis of dynamic structures (FADS) was found to be unsuccessful due to the small size of the cardiac chamber that causes extensive mixture of TACs of different structures. **Methods:** In this study, we used digital phantoms of the left ventricle (LV cavity size: 1-2 cm) and small monkey (LV cavity size: ~ 2 cm) dynamic FDG PET studies to evaluate FADS for extracting the pure blood-pool TACs by adding a single blood sample (taken at a late scan time) constraint. **Results:** In the digital phantom studies, spillover fractions in the extracted blood-pool TACs using FADS without a blood sample constraint (FADS(-)) and with a blood sample constraint (FADS(+)) were 3%-

91% and < 3%, respectively. In the monkey studies (n = 4), FADS(+) extracted blood-pool TACs matched well with the arterialized well counter measurements (% differences of curve integration: FADS(-) < 82%; FADS(+) < 9%). The microparameters (K_1^* , k_2^* , k_3^* , k_4^*) and macroparameters (K_{tr}), obtained from the FADS(+) blood-pool TACs, were similar to those obtained from plasma samples in a three-compartment model fitting (% differences of K_{tr} : phantom studies < 5%; monkey studies < 9%). **Conclusion:** The FADS technique with a single-blood sample has the potential to extract the pure blood-pool TACs directly from dynamic PET images of a small animal without multiple blood sampling, region of interest definition or spillover correction.

Key Words: factor analysis; blood-pool time-activity curve extraction; PET; fluorine-18-FDG

J Nucl Med 1996; 37:1717-1722

Received July 10, 1995; revision accepted Feb. 28, 1996.

For correspondence or reprints contact: Sung-Cheng Huang D.Sc., Division of Nuclear Medicine and Biophysics, Department of Molecular and Medical Pharmacology, UCLA School of Medicine, 10833 Le Conte Ave., Los Angeles, CA 90095-6948.

The feasibility of extracting pure arterial time-activity curves (TACs) from human adult dynamic 2-[¹⁸F]fluoro-2-deoxy-D-glucose (FDG) PET images using factor analysis of dynamic structures (FADS) was demonstrated in a previous study (1). However, our study in dynamic PET images of a small animal heart showed that the separation of the pure arterial TAC using FADS was unsuccessful due to the small size of the cardiac chamber that causes extensive mixture of TACs of different structures.

As described by Barber and Di Paola et al., the kinetics of *n* factors were searched as *n* apex points on an *n*-1 factorial subspace within a positivity area (2,3). The estimation of the apex points [i.e., B matrix in FADS algorithm; for detail, see Di Paola et al. (3)] was done through an iterative algorithm and weighted toward dixels (TAC on a pixel basis) with little or no contribution from other dynamic structures. Therefore, dixels lacking pure physiological factors due to limits in image resolution or coarse image resampling may cause errors in the estimation of *n* physiological factors in small objects (1). Due to this limitation, we studied further improvement in FADS, as it is applied to small hearts.

This study was confined to FADS of *n* = 2 physiological factors. If a dynamic sequence contains two well-separated structures (e.g., ventricular cavity and myocardial wall) which are defined by two different kinetics (e.g., ventricular blood-pool and myocardial tissue TACs), then the two physiological factors can be estimated using FADS by finding two extreme points on a one-dimensional factorial subspace as described by Barber et al. (2). However, if limited PET scanner resolutions cause extensive mixing of the TACs of the two structures (i.e., no pure dixels), the extreme points estimated by FADS may be two points which are located somewhere between the true endpoints along the one-dimensional factorial subspace. The present study evaluates a method to iteratively adjust the apex points from FADS outwardly so that the new FADS blood-pool TACs are under an additional constraint (i.e., a blood sample count at a late scan time). We hypothesize that on digital phantoms of LV and monkey FDG PET dynamic studies, the accuracy of FADS blood-pool TACs can be improved using FADS with a blood sample constraint (FADS(+)). Furthermore, the effect of error in the estimation of the input function on quantitative parameters of FDG studies is minimal.

MATERIALS AND METHODS

FADS With and Without Blood Sample Constraints

Figure 1 depicts the procedures we used in FADS techniques with and without a blood sample constraint. The procedures used to estimate the FADS blood-pool TAC without a blood sample constraint (FADS(-)) was described in detail in a previous study (1). The estimation of the first B matrix was described in detail by Di Paola et al. (3). After generating the FADS(-) blood-pool TAC (i.e., the FADS blood-pool TAC obtained from the first B matrix of Fig. 1, which met the positivity constraints only), the FADS(-) blood-pool TAC was compared to the blood sample constraint. The iterations for adjusting the value in the B matrix (with smallest step size = 0.0001) continued until the FADS(+) blood-pool TAC (i.e., the FADS blood-pool TAC that met the blood sample constraint and the positivity constraints) was found. In each B matrix iteration, only the apex corresponding to the blood-pool TAC was adjusted (i.e., adjust the FADS estimated apex point outward along the one-dimensional factorial subspace). The apex corresponding to the myocardial tissue factor was fixed at the same value from the first B matrix iteration.

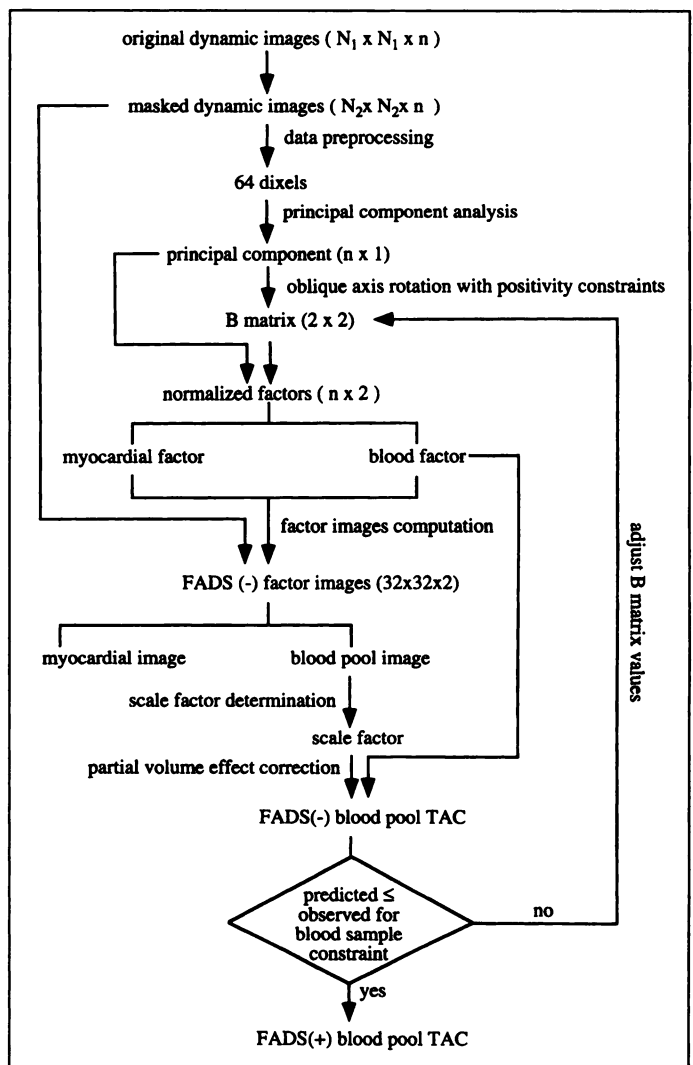


FIGURE 1. Flowchart of FADS technique with and without a single blood sample constraint. FADS(-) blood-pool TAC is obtained after the first iteration of B matrix. FADS(+) blood-pool TAC is obtained after B matrix iterations and meet the blood sample constraint.

Digital Phantom Studies

Dynamic 65-min animal PET scans of left ventricle were simulated: 24 frames with nine 10-sec, seven 30-sec, two 300-sec and six 500-sec scans, respectively. These dynamic phantoms were forward projected to sinograms (32 linear samples; 2 mm/pixel; 3.3 mm/plane; 80 angles) of two digital phantoms (I and II). Each phantom was constructed based on two slightly eccentric ellipses of different sizes (configuration is shown in Fig. 2) but similar to the heart sizes (cavity size and tissue thickness) found in the monkey studies (Tables 1, 2). The kinetics of the LV blood pool and myocardium were simulated using an arterial plasma TAC from a monkey study and a myocardial tissue TAC (Fig. 3A) mathematically derived from a three-compartment FDG model with rate constants from a human volunteer ($K_1^* = 0.41$ ml/min/g, $k_2^* = 0.63$ min⁻¹, $k_3^* = 0.10$ min⁻¹ and $k_4^* = 0.0032$ min⁻¹). For each phantom, three dynamic sinograms were simulated: LV blood-pool activities alone; myocardial tissue activities alone; and both LV blood-pool and tissue activities. The sinograms were smoothed in both the in-plane and axial directions (4.4 and 3.3 mm FWHM, respectively). Poisson noise equivalent to a 10⁶ cts/scan was added to each sinogram. Short-axis images were reconstructed into a 32 × 32 matrix (2 mm/pixel), with a 3.3-mm plane separation. These images were reconstructed to yield in-plane and axial spatial resolutions comparable to those of current PET

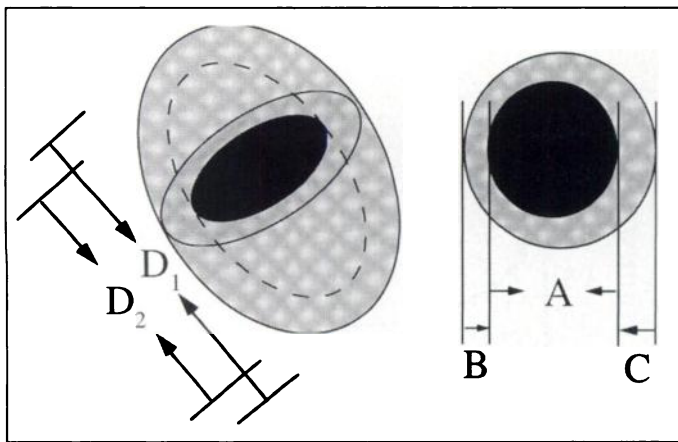


FIGURE 2. Configurations of LV digital phantom. Digital phantom sizes (A, B, C, D₁ and D₂) are listed in Table 1. Short-axis LV images were reconstructed from the lower half of the two ellipses.

scanners (4.4 and 3.3 mm FWHM, respectively). In this study, only three image planes were evaluated: plane I_a and plane I_b from phantom I; plane II_a from phantom II (sizes are listed in Table 1). FADS techniques, with or without a blood sample constraint (counts of the blood sample taken at 35.8 min, which is equivalent to the midscan time of frame 21 in dynamic sequence), were then applied to the dynamic images to evaluate the performance of the algorithms (Fig. 1). Due to partial volume effects, the magnitude of the FADS blood-pool TACs of plane I_b and plane II_a were corrected with recovery coefficients (plane I_b: 0.80; plane II_a: 0.78, which were calculated from the ratio of counts in the pure blood-pool simulations and true plasma counts) before comparing to the blood sample counts in each B matrix iteration (Fig. 1).

Monkey FDG-PET Studies

Four FDG-PET dynamic studies were performed in four monkeys (weight range: 2.3–5.8 kg; mean left ventricular dimension: 14.9–18.5 mm) (Table 2). Myocardial dimensions (wall thickness and cavity size) were determined with m-MODE echocardiogram using an ACUSON 128 (Mountain View, CA) and a 7.5-MHz transducer. All the monkeys were fasting. After intravenous injection of FDG (mean dose = 6.7 mCi), dynamic images were obtained with an animal PET scanner. The dynamic sequence consisted of nine 10-sec, seven 30-sec, two 300-sec and three 500-sec scans for a total scan time of 40 min. Photon attenuation was corrected with a 20-min transmission scan using a ⁶⁸Ge/⁶⁸Ga external ring source. The 128 × 128 transaxial images (3.4 mm thick) were reconstructed using a Shepp-Logan filter with a cutoff frequency of 0.5 Nyquist frequency, resulting in an in-plane spatial resolution of ~ 4.4 mm FWHM. The 15 contiguous transaxial images of each study were then reoriented into six left ventricular

TABLE 1
Sizes of Left Ventricle and Short-Axis Images Digital Phantoms

	A (mm)	B (mm)	C (mm)	D ₁ (mm)	D ₂ (mm)
Phantom I	20*	4.0*	4.4*	56.8*	40*
Phantom II	10*	1.7*	1.8*	27.0*	20*
Plane I _a †	20	4.0	4.4		
Plane I _b †	12.8	6.8	7.2		
Plane II _a †	10	1.7	1.8		

*These values were measured at the center of each ellipse. Therefore, the chamber sizes and thicknesses of myocardium in different short-axis images may differ from these values (e.g., plane I_b).

†Plane thickness: 3.3 mm.

TABLE 2
Data for Monkeys Who Had FDG-PET Studies

Monkey no.	Age (days)	Sex	Weight (kg)	LV chamber (mm)*		LV walls (mm)*	
				ED†	ES†	Septum	Lateral
1	1394	M	5.75	21.6	15.3	2.9	2.8
2	2808	F	5.30	21.5	15.5	2.3	2.4
3	462	M	2.30	18.0	11.7	2.3	2.4
4	1262	M	5.50	20.3	14.7	3.9	4.4

*Measured by echocardiogram.

†Ed = end-diastolic; ES = end-systolic.

short-axis images as described previously (4). The short-axis dynamic images of a midventricular plane (plane 3 of the six contiguous short-axis images in each study) were submitted to the FADS with or without a blood sample constraint. Dixel sizes for Monkeys 1 and 2 were 31.2 mm² and 7.8 mm² for Monkeys 3 and 4. The blood sample was taken ~ 27.5 min after FDG injection, which is the midscan-time of frame 20 in the dynamic sequences. The first two factors, which accounted for ~75% (or greater) of total variance, were extracted. In addition, the arterial bloods samples were taken at ~30-sec intervals over the first 4 min and at progressively lengthening intervals for the remaining duration of the scan (~ 20 samples/40-min study).

Validation of the FADS Blood-Pool TACs

To validate the replacement of blood sampling with FADS generated blood-pool TACs, we compared the FADS blood-pool TACs with arterial plasma samples and a region of interest (ROI) generated LV blood-pool TACs. The accuracy of blood TACs was also evaluated by using the different blood TACs as input functions to estimate the glucose metabolic rate constant, macroparameter K(ml/min/g), using a three-compartment FDG model (5,6) or Patlak graphical analysis (7). A blood volume term was included in the three-compartment model (8).

Sensitivity of the quantitative glucose metabolic estimates to error in the counts of the single blood sample constraint was evaluated by adding ± 2%, 5%, 10%, 15% and 20% of errors to the blood sample count. The FADS(+) blood-pool TACs were derived

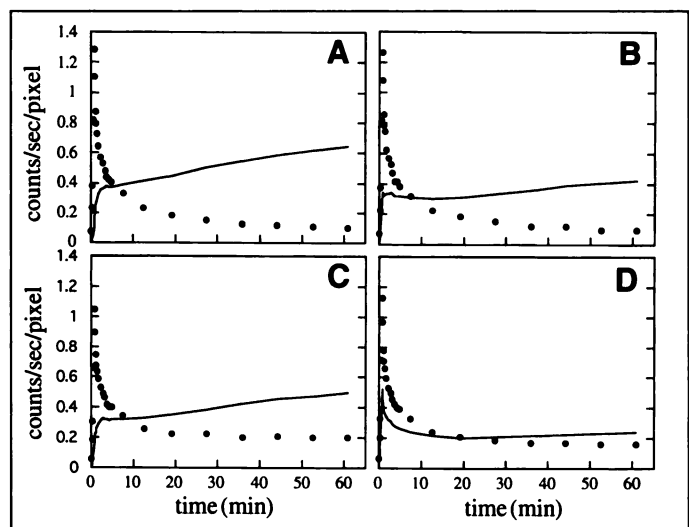


FIGURE 3. (A) Plasma samples (solid circles) and simulated myocardial tissue TAC (line) which were used to generate the dynamic phantom sinograms. (B, C, D) ROI-derived LV blood-pool (solid circles; ROI ~ 3 mm²) and tissue (line; ROI ~ 15 mm²) TACs from the three dynamic short-axis images of digital phantoms ((B) plane I_a; (C) plane I_b; (D) plane II_a; sizes are listed in Table 1).

from the dynamic phantom images II_a and the blood sample constraint using different errors ($\pm 0\%$ – 20%). The integrated blood TAC, K_{nir} (ml/min/g), K_{pat} (ml/min/g), using the FADS(+) blood-pool TACs were then compared to those obtained using the true plasma curve as the input function.

RESULTS

Digital Phantom Studies

Figure 3B–D shows the ROI-derived blood-pool and tissue TACs (blood-pool ROI $\sim 3 \text{ mm}^2$; tissue ROI $\sim 15 \text{ mm}^2$) from planes I_a , I_b and II_a from the digital phantoms of various sizes which contain ventricular blood-pool and myocardial tissue activities (Table 1). For a smaller cardiac chamber (i.e., planes I_b and II_a , Fig. 3C, D), the blood-pool TACs had lower counts at the peaks due to partial volume effects and higher counts at the tails due to the myocardial tissue spillover activities. The point-to-point percent differences of ROI-derived blood-pool TACs compared to the true plasma TAC were calculated. More than 50% spillover fractions [calculated as $((\text{LV blood-pool count} - \text{plasma count})/\text{plasma count}) \cdot 100\%$] existed when mid-scan-times were larger than 35 min in image sequences of planes I_b and II_a . The ROI-derived myocardial tissue TACs (Fig. 3B, C and D from phantom image planes I_a , I_b and II_a , respectively) had lower counts and an earlier peak, which were different from those in the original myocardial tissue TAC (Fig. 3A) due to partial volume effects and blood-pool spillover activities.

Figures 4A–C show the FADS(-) and FADS(+) blood-pool TACs extracted from phantom images I_a , I_b and II_a , respectively. For a large cardiac chamber, both the FADS(-) and FADS(+) blood-pool TACs (plane I_a , Fig. 4A) were similar to the true plasma input function. However, the FADS(-) blood-pool TACs contained large amounts of myocardial spillover activities when cardiac chambers were small relative to the image resolution (planes I_b and II_a , Figs. 4B and C). The average percent spillover activity (from 5–65 min) of FADS(-) blood-pool TACs from plane I_a , plane I_b , plane II_a are $\sim 3\%$, $\sim 91\%$ and $\sim 55\%$, respectively. However, the average percent spillovers (from 5–65 min) in the FADS(+) blood-pool TACs from plane I_a , plane I_b , plane II_a are $\sim 3\%$, $\sim 1\%$ and $\sim 2\%$, respectively. Table 3 shows the quantitative estimates of myocardial glucose metabolism using the plasma curve and FADS(+) blood-pool TACs as the input function. Integrated from 0 to 65 min and compared to the area under the plasma curve, the FADS(+) blood-pool TACs had errors of $\leq 2\%$. The microparameters (K_1^* , k_2^* , k_3^* , k_4^*) and macroparameters (K_{nir} or K_{pat}), obtained by using the FADS(+) blood-pool TACs, were similar to those obtained by using the plasma curve in a three-compartment model fitting (5,6) or Patlak graphical analysis (7) (% differences: $K_{nir} < 5\%$; $K_{pat} < 3\%$).

The study of error ($\pm 0\%$ – 20% counts) in the FADS(+) blood sample constraint showed that the errors in glucose metabolic rate constants, K_{nir} and K_{pat} , were nonlinearly proportional to the magnitudes of the errors in the blood sample constraint. When $\leq 5\%$ of errors were added to the count of the blood sample constraint, the errors of the blood curve areas, the K_{nir} and K_{pat} estimates were within 3%, 4% and 4%, respectively.

Monkey FDG-PET Studies

Figure 5 shows the ROI ($3\text{--}6 \text{ mm}^2$)-derived LV blood-pool TACs, the FADS(-) and FADS(+) blood-pool TACs extracted from the three monkey dynamic FDG-PET images (results of Monkey 1 were similar to Monkey 2). These LV blood-pool TACs were noisy with or without myocardial spillover activities (average % differences compared with arterial blood samples from 5 to 40 min: $\sim 7\%$ Monkey 1; $\sim 3\%$ Monkey 2;

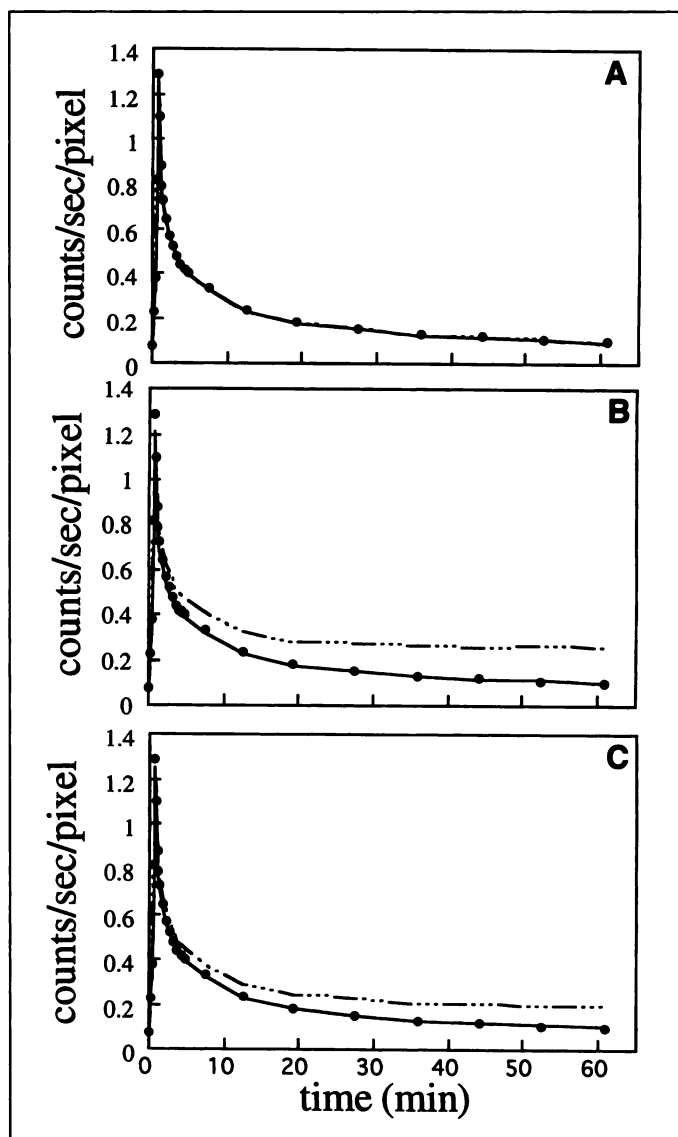


FIGURE 4. Comparison of the plasma curve (solid circles) with the FADS(-) (line with dots) and FADS(+) (line) blood-pool TACs extracted from the three dynamic phantom images (A) plane I_a ; (B) plane I_b ; (C) plane II_a).

$\sim 89\%$ Monkey 3; $\sim 100\%$ Monkey 4). When there was no or little myocardial uptake (e.g., Monkey 2 or Monkey 1) (Fig. 5A), the FADS(-) blood-pool TAC was similar to the plasma curve (average % differences compared with plasma samples from 5 to 40 min: $\sim 7\%$ Monkey 1; $\sim 6\%$ Monkey 2). These results show that a blood sample constraint may not be necessary for FADS to extract the pure blood-pool TAC when there is very little myocardial tissue activity present in the original images. However, when myocardial uptakes were relatively high, the FADS(-) blood-pool TACs contained large amounts of spillover from myocardial activities (% differences: $\sim 37\%$ Monkey 3; $\sim 82\%$ Monkey 4) (Figs. 5B, C). When a blood sample constraint was added, the FADS(+) blood-pool TAC improved and had less spillover activity (% differences: $\sim 9\%$ Monkey 3; $\sim 2\%$ Monkey 4).

Table 3 shows the quantitative estimates of myocardial glucose metabolism using plasma samples and FADS(+) blood-pool TACs as input functions in the monkey studies. The myocardial tissue TAC of each monkey study was generated from a myocardial tissue ROI and the short-axis dynamic images. Since there was minimal myocardial uptake in Monkeys 1 and 2, only the data from Monkeys 3 and 4 were

TABLE 3

Quantitative Estimates of Myocardial Glucose Metabolism Using FADS(+) Blood-Pool TACs or Plasma Curve as the Input Function in Phantom and Monkey Studies

	Input function	Curve integration ^a	K_1^* (ml/min/g)	k_2^* (min ⁻¹)	k_3^* (min ⁻¹)	k_4^* (min ⁻¹)	K_{nir}^\dagger (ml/min/g)	K_{pat}^\ddagger (ml/min/g)
	Plasma	1.00	0.41	0.63	0.10	0.003	0.0562	0.0518
Plane I _a	FADS(+) TAC	0.98	0.42	0.63	0.10	0.003	0.0573	0.0532
Plane I _b	FADS(+) TAC	0.98	0.44	0.64	0.10	0.004	0.0587	0.0531
Plane II _a	FADS(+) TAC	1.00	0.43	0.64	0.10	0.004	0.0576	0.0521
Monkey 3 [§]	Plasma	1.00			0.09	0.0	0.022	0.022
	FADS(+) TAC	1.04			0.10	0.003	0.023	0.022
Monkey 4 [§]	Plasma	1.00			0.32	0.025	0.236	0.146
	FADS(+) TAC	1.04			0.27	0.022	0.217	0.143

[†]Macroparameter, K, estimated from a three-compartment model (7-10); $K_{nir} = K_1^* \cdot k_3^* / (k_2^* + k_3^*)$.

[‡]Macroparameter, K, estimated from Patlak graphical analysis (9).

[§]Tissue curves were generated from a myocardial tissue ROI and the short-axis dynamic sequence.

^aRatio of areas under the FADS(+) blood-pool TACs and plasma curve; integration time: phantom study: from 0 to 65 min; monkey study: from 0 to 40 min.

estimated. The integrated area (0-65 min) using the FADS(+) blood-pool TACs had a $\leq 4\%$ difference compared to the area under the arterial plasma curve. The microparameters (e.g., k_3^*

and k_4^*) were more sensitive to the input functions. The macroparameters, K_{nir} and K_{pat} , estimated using the FADS(+) blood-pool TACs and the plasma curve had differences $\leq 9\%$ and $\leq 3\%$, respectively.

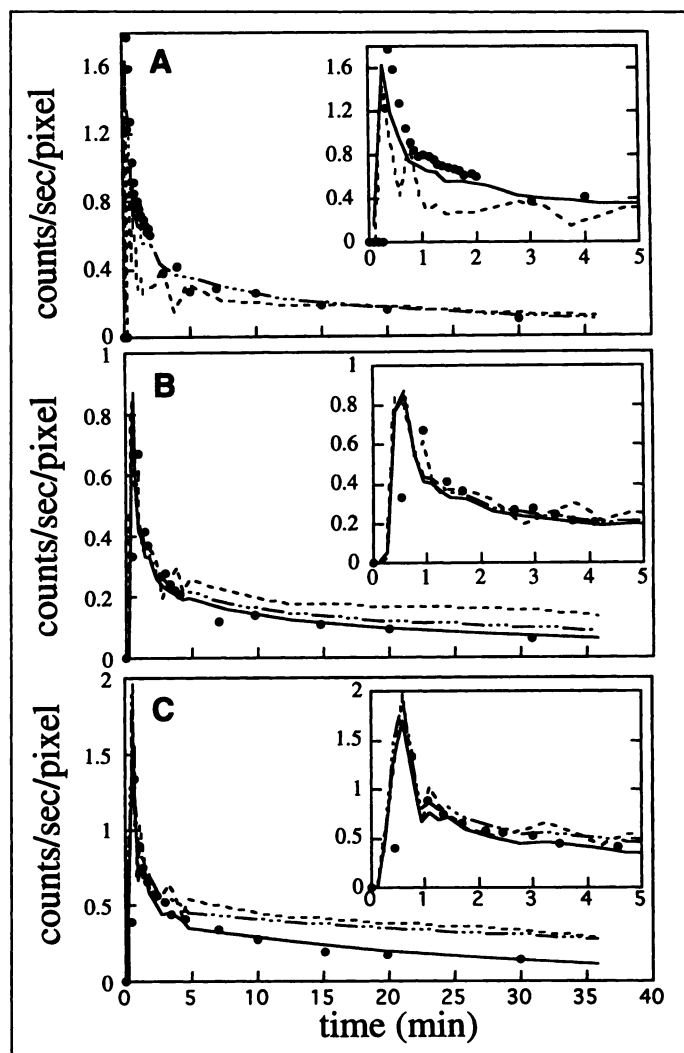


FIGURE 5. Comparison of the plasma samples (solid circles) with ROI-derived LV blood-pool TACs (dash line, ROI 3-6 mm²), the FADS(-) (line with dots) and FADS(+) (line) blood-pool TACs extracted from the monkey FDG PET dynamic studies ((A) Monkey 2; (B) Monkey 3; (C) Monkey 4).

DISCUSSION

Quantitative FDG-PET studies performed in animals serve as an important model for evaluating the kinetics of human glucose metabolism. The LV blood-pool TACs may contain large amounts of spillover activities from the adjacent structures (e.g., myocardial tissue activity) due to the limited image resolution relative to the small animal hearts. Therefore, the quantitative estimates obtained by using the ROI-derived LV blood-pool TACs as input functions may not be reliable.

One of the limitations of the FADS technique in extracting pure blood-pool TACs in dynamic PET studies of relatively small cardiac chambers is the need for a pure blood-pool dixel in the dynamic image sequence. In addition, the image condensing procedure (i.e., increased dixel area) was often performed in the FADS techniques to improve the signal-to-noise ratio and to decrease the computation time. In our monkey studies, it took 10-30 sec when 64 dixels were submitted to the FADS for a two-factor extraction (MATLAB[®] implemented on a SPARC[®] 10 SUN workstation). Therefore, the absence of a pure dixel in the original dynamic sequence or very coarse resampling relative to the image resolution may cause errors in the estimation of physiological factors. Similar errors were found in scintigraphic dynamic studies, and refinements of FADS techniques have been proposed (9-11). These methods used an additional constraint in the form of a compartmental model to determine a specific physiological factor for a structure of interest. The limitations of this method are the availability of a reliable theoretical model to describe a particular structure in the study and the ability to estimate only one physiological factor (11).

Other investigators have estimated myocardial spillover activities in blood-pool TACs with a method that uses the crosstalk of activities from one or two dimensions within the planar image (12). This method did not account for spillover activities from the axial direction. For a small heart and a limited axial resolution, the spillover activity due to the overlap of blood-pool and myocardium may not be ignored. Since FADS assumes that the signal measured at each dixel is a

weighted sum of the underlying kinetics, it is not limited by the source(s) of the spillover activities.

This study shows that if the cardiac chamber is large (e.g., > 2 cm) and if there is no myocardial uptake, a blood-pool TAC similar to the plasma samples could be found near the center of the LV chamber without additional correction (Figs. 4A and 5A). However, even though the LV sizes (~ 2 cm) were not extremely small compared to the scanner resolution (FWHM ~ 4.4 mm), various error sources and significant myocardial uptake caused the extraction of the pure blood-pool TACs from FADS to be unsuccessful (Figs. 4B, 4C, 5B, 5C). The errors included heart movements, limited in-plane and axial scanner resolutions, noise and high FDG uptake in the surrounding tissues, etc. The results in this study validated the reliability and accuracy of FADS(+) blood-pool TACs obtained from small hearts (e.g., LV size 1–2 cm diameter) (Table 3; Figs. 4B, 4C, 5B and 5C). Although improvement of FADS(+) myocardial tissue factors were not considered and remained the same as FADS(-) myocardial tissue factors in the method (for detail, see Materials and Methods), the results showed that FADS(+) blood-pool TACs were improved and accurate enough for use as input functions. Furthermore, the arterial blood sample used in this study may ultimately be replaced by a hand-warmed venous blood sample if the counts are similar at late scan times (5).

Since only a single-blood sample was used as a constraint to evaluate the entire blood curve, there are factors that could affect the accuracy of FADS(+) blood-pool TACs. These factors include errors in blood sample counts, noise and partial volume effects in the dynamic sequences. The phantom study showed that the FADS(+) method was not sensitive to errors in the blood sample counts. If there were $\leq 5\%$ of errors in the blood sample counts, the errors of the K_{nlr} and K_{pat} estimates were $\leq 4\%$. In the program we implemented, we smoothed the FADS blood-pool TAC at the last five time points in each B matrix iteration (Fig. 1) before comparing to the blood sample constraint. This procedure could minimize the noise or errors in the dynamic images. The errors might be due to movement at a particular scan time (i.e., at the time the blood sample was taken). Furthermore, if the cardiac chamber is small relative to the image resolution (e.g., the cardiac chamber is smaller than 2 FWHM of the scanner resolution), partial volume effects may decrease the counts in the image (13). Therefore, the counts in the FADS blood-pool TAC were corrected for partial volume effects (e.g., planes I_b and II_a of the phantom studies, Materials and Methods) before comparing to the blood sample counts. Correlation and registration of PET results with anatomic imaging modalities such as MRI and CT will permit direct measurements of the recovery coefficients (the fraction of true counts recovered in a given ROI) (14). Furthermore, if PET and MR images are acquired in gated mode, lessened effects of heart movement may increase the accuracy of the FADS technique. Since the cardiac chambers of the monkeys in this study were relatively large (~ 2 cm, which is comparable to the chamber size of plane I_a of the phantom study), the partial volume effect corrections were ignored in the monkey studies.

The results showed that the FADS(+) blood-pool TAC were sufficiently accurate to replace the plasma curves in the quantitative studies (Fig. 5, Table 3). Because of whole blood activities in FADS blood-pool TACs, the FADS technique is suitable as long as there is a fixed ratio of tracer concentration between whole blood and plasma. However, if FDG metabolism is found in the blood cells, metabolite correction in blood needs to be considered.

CONCLUSION

We have demonstrated that a single-blood sample constraint improved the accuracy of the FADS technique in extracting a pure blood-pool TAC for dynamic PET studies that have large spillover problems. Therefore, the FADS technique with a blood sample can potentially extract pure blood-pool TACs directly from dynamic PET images of a small animal without multiple blood samples, ROI definition or spillover correction.

ACKNOWLEDGMENTS

We thank the UCLA cyclotron staff for synthesizing the FDG compounds used in this study, Ron Sumida and the UCLA PET scanner staff for performing the PET studies and Drs. E. J. Hoffman, M. Dahlbom, A. R. Ricci, K. Gardner and D. Truong for instrumentation, computer hardware and software support. This work was partly supported by Department of Energy grant DE-SC03-87ER60615 and AHA-Greater LA Affiliate, Investigative group fellowship 617.IG-15.

REFERENCES

1. Wu HM, Hoh CK, Choi Y, et al. Factor analysis for extraction of blood time-activity curves (TACs) in dynamic PET-FDG studies. *J Nucl Med* 1995;36:1714–1722.
2. Barber DC. The use of principal components in the quantitative analysis of gamma camera dynamic studies. *Phys Med Biol* 1980;25:283–292.
3. Di Paola R, Bazin JP, Aubry F, et al. Handling of dynamic sequences in nuclear medicine. *IEEE Trans Nucl Sci* 1982;NS29:1310–1321.
4. Kuhle WG, Porenta G, Huang SC, et al. Issue in the quantitation of reoriented cardiac PET images. *J Nucl Med* 1992;33:1235–1242.
5. Phelps ME, Huang SC, Hoffman EJ, Selin CJ, Sokoloff L, Kuhl DE. Tomographic measurement of local cerebral glucose metabolic rate in humans with (F-18) 2-fluoro-2-deoxy-D-glucose: validation of method. *Ann Neurol* 1979;6:371–388.
6. Huang SC, Phelps ME, Hoffman EJ, et al. Noninvasive determination of local cerebral metabolic rate of glucose in man. *Am J Physiol* 1980;238:E69–E82.
7. Patlak CS, Blasberg RG, Fenstermacher JD. Graphical evaluation of blood-to-brain transfer constants from multiple-time uptake data. *J Cereb Blood Flow Metab* 1983;3:1–7.
8. Hawkins RA, Phelps ME, Huang SC. Effects of temporal sampling, glucose metabolic rates and disruptions of the blood-brain barrier on the FDG model with and without a vascular compartment: studies in human brain tumors with PET. *J Cereb Blood Flow Metab* 1986;6:170–183.
9. Houston AS. The effect of apex-finding errors on factor images obtained from factor analysis and oblique transformation. *Phys Med Biol* 1984;29:1109–1116.
10. Nijran KS, Barber DC. Towards automatic analysis of dynamic radionuclide studies using principal-components factor analysis. *Phys Med Biol* 1985;30:1315–1325.
11. Nijran KS, Barber DC. Factor analysis of dynamic function studies using a priori physiological information. *Phys Med Biol* 1986;31:1107–1117.
12. Henze E, Huang SC, Rabbit O, et al. Measurements of regional tissue and blood-pool radiotracer concentrations from serial tomographic images of the heart. *J Nucl Med* 1983;24:987–996.
13. Hoffman FJ, Huang SC, Phelps ME. Quantitation in positron emission computed tomography. 1. Effect of object size. *J Comput Assist Tomogr* 1979;3:299–308.
14. Hawkins RA, Choi Y, Huang SC, et al. Quantitating tumor glucose metabolism with FDG and PET [Editorial]. *J Nucl Med* 1992;33:339–344.